Development of a dual optical fiber probe for the hydrodynamic investigation of a horizontal annular drive gas/liquid ejector

Aliyu Musa Aliyu[1], Yoon Kee Kim[1], Seong Hwan Choi[1], Joo Ha Ahn[2], Kyung Chun Kim[1*]

[1] School of Mechanical Engineering, Pusan National University, San 30, Jangjeon-dong, 609-735, Busan, Republic of Korea

[2] Technical Research Department, Tanktech Co. LTD., Busan, 618-817, Korea

Abstract

A dual-channel optical fiber probe was developed to quantify the bubble characteristics (void fraction, velocity, and bubble size) in a gas–liquid annular ejector system. Water is pumped upstream of the ejector contraction. Since a low pressure region exists downstream in the ejector diffuser, this permits air to be sucked into the flowing liquid by jet pump action and the inlet air volumetric flow rate is measured by a flow meter. Verification of the void fraction (range 0.15 – 0.5) measured by the optical fiber probe was then possible and deviations were generally around ± 5 %. Also, bubble velocity was measured using the optical probe by cross-correlating signals from the two fibers whose tips are separated by a known distance. Alternatively measuring bubble velocity using a particle image velocimetry method provided validation for the optical fiber probe system where a high speed camera was used to capture instantaneous bubble images at time intervals of 0.125 ms. Excellent agreement between the velocities using both methods is reported. For bubble size measurements, analyzing the temporal signals from a single probe enabled estimation of the size of a bubble. Bubble sizes measured ranged between 1.5 and 6.0 mm and size distributions were constructed for different ejector water volumetric flow rates ranging from 0.0022 to 0.0063 m^3/s. LabVIEW provided a convenient platform for coding the algorithms for estimating the void fraction, bubble velocity and bubble size. For further comparison, a CFD study of the ejector system was done, and the vertical radial profiles of the void fraction were compared with those obtained by the optical fiber system and these showed good agreement.

Keywords: Fiber optic probe, Fresnel reflection, bubbly flow, annular ejector, void fraction, CFD.

1 Introduction

Measurements of local flow characteristics in gas–liquid systems are important for both their design and operation. Of particular importance are industrial applications where bubbly flow occurs due to the high mass transfer and reaction rates that can occur during gas–liquid contacting. Examples of such applications in industry include absorption and stripping [1], aerobic biochemical reactors for large-scale waste water treatment plants [2], hydrogen recirculation devices in proton exchange membrane

fuel cell (PEMFC) systems [3], and vapor compression refrigeration systems [4]. Nowadays, preliminary designs using computational fluid dynamics simulations are increasingly being carried out, and information on bubble interfacial area is needed. Therefore, knowledge of bubble properties such as void fraction, bubble velocity, and bubble size distribution are of utmost importance.

In a brief review for their paper, Mizushima et al. [5] noted that over the years, many methods have been devised for the measurement of bubble characteristics in multiphase flows. These include measuring void fraction by the level of an aerated liquid in comparison with the single phase liquid in a bubble column [6]; high-speed photography and image processing [7]–[9] for bubble rise velocity, mean diameter, and low void fractions respectively. Others are double sensor conductivity probes for bubble velocity and interfacial area concentration measurements [10]; gas holdup, bubble size and shape distribution using laser Doppler anemometry [11]; bi-optical fiber technique for low bubble velocity in an airlift column [12]; and highly intrusive wire mesh sensors for bubble void fraction measurements in conduit flows developed [13]–[15].

Serious complications can occur in measuring bubble characteristics while flowing such as intrusiveness, bubble distortion, and temporal resolution for high velocity bubbly flow. Use of optical fiber probes is one very promising technique that can satisfactorily reduce these shortcomings due to its high sensitivity to local phase changes that have different refractive indices. Indeed since the measuring principle of optical fibers governed by Snell's law was introduced to bubbles [16], both mono- and multi-fiber systems have been widely used in gas–liquid systems across chemical process and nuclear applications. For example [17] measured the local gas-phase characteristics in a bubble column in the presence of paraffin oil and nitrogen at high temperatures (T = 100–175 °C) using a mono-optical fiber probe at low gas velocities of between 0.02 and 0.15 m/s. Xue et al. [18] used four-point optical probes to obtain the bubble velocity vectors and bubble size using the calibration technique between the probes and a charge-coupled device (CCD) camera to correct for bubble distortion. However, while the likely obtrusiveness of a four-probe system exists, it was not clear from their study its ability to adequately measure high velocity bubbly flows. Enrique Julia et al. [19] investigated the accuracy of the fiber optic probe vis-à-vis its distorting, and non-perpendicular piercing effect on the bubbles. A synchronized high speed camera was used with bubble velocities of 0.22–0.28 m/s. No specific application was mentioned and a correction method was not proffered.

From the foregoing while a variety of systems have been used, and various corrections applied to cater for bubble distortion, it is evident optical fiber application to relatively high velocity bubbly flows e.g. finely dispersed bubbly flow has not been reported in the open literature where mixture velocities can approach 5 m/s. One of such applications is in gas/liquid ejectors where a high velocity liquid is pumped through a conduit which has a venturi-type constriction. Ejectors utilize a high speed fluid jet as a pumping resource to entrain a secondary phase (e.g gas) into the suction chamber. Pumping

of the secondary fluid is possible because a low pressure region is formed downstream the ejector expansion region at high velocities, and the secondary fluid is hence sucked into this region. Ejectors have found wide applications in liquid–liquid and gas–liquid contacting systems such industrial units in mixer/settler systems, micro- and milli-bubble formation for water treatment and turbulence enhancers in bubble column reactors, and heat transfer applications.

In this study, a hydrodynamic investigation was performed on an annular drive gas/liquid ejector using a dual optical fiber probe specifically developed to measure the bubble characteristics (void fraction, velocity, and bubble size). The gas superficial velocities were between 0.6–1.8 m/s in a 65 mm internal diameter horizontal pipe. Verification of the void fraction and bubble size distributions was carried out using alternative methods, as well as the bubble velocity. For comparison purposes, a CFD study of the ejector system is also performed, and the vertical profiles of the void fraction obtained are compared with those obtained by the optical fiber system.

2 Measuring principle of the optical fiber

The optical fiber probe system was developed to estimate the local void fraction, bubble velocity and bubble diameter. The measuring principle is based on the Fresnel reflection occurring at the interface between the two media with different refractive indices [20]. Therefore the Fresnel coefficient at the tip of the probe is dependent upon the refractive index of each phase; and for normal light incident at an interface between air and water with refractive indices of n_1 and n_2 respectively, the Fresnel coefficient *R* is given by:

$$R = \left(\frac{n_1 - n_2}{n_1 + n_2}\right)^2 \quad \textbf{(1)}$$

For an air–water mixture together with a fiber index of $n_1 = 1.46$, the following Fresnel coefficients are obtained:

$R_{g-a} = 3.5\%\ \ (glass - air)$

$R_{g-w} = 0.2\%\ \ (glass - water)$

$R_{w-a} = 2.0\%\ \ (water - air)$

According to the Fresnel reflection, approximately 3.5% of the incident light is reflected backward to the interface between glass and air, but less than 0.2% of incident light is reflected at the interface between glass and water; and 2% is reflected at the air–water interface. When the tip of the probe is in contact with water, R is approximately 17.5 times higher than when it is in contact with air. Therefore, the amount of light reflected changes with the change in the medium in contact with the probe. The voltage level was thereafter detected using the changes recorded by the photodetector, and the signal

difference can be used for estimating the void fraction. The illuminated light from the light source and the reflected light at the tip of the probe along the water-air interfacial plane reached the optical fiber probe and the photodetector, respectively, through the beam coupler. The light reaching the photodetector was estimated as an electronic signal voltage, and this voltage data was acquired by the DAQ board and stored in the computer in real-time. High temporal/spatial resolution and stability of the output signal are the key advantages of measuring the void fraction using an optical fiber probe.

3 Probe fabrication

The optical fiber used was FOSTEC 3.0 mm Type OFNR, with 125 μm and 50 μm cladding and core diameters respectively. The tip of the probe was fabricated using precision hand-held Thorlabs fiber stripper and cleaver devices (shown in Figure 2) to remove the outer buffer regions, and cut the tip perpendicular to the fiber axis.

Figure 1: Hand-held precision tools for optical fiber probe fabrication

A micro-grinder/microscope device was used to inspect and finely finish the exposed optical fiber ends to ensure good quality signals are obtained. These were carefully mounted as a pair in a 20G hypodermic steel pipe, which was in turn inserted to a 1/16-inch pipe and epoxy glue was applied to hold them in place. Finally, they were glued in a 1/8-inch pipe to form a solid probe assembly. The distance between the two exposed probe tips Δh was measured under a microscope as shown in Figure 2. As the size of the probe was very small, measuring the distance accurately was difficult. In advance, we captured a calibration image with a superimposed ruler and the probe under the microscope. This enabled the distance per pixel of the image to be calculated. Using image-processing software, the separation between the two probe tips was determined in pixels, and this was converted to micrometers using the μm/pixel calibration value. This was done three times and a mean value obtained. For the probes used in the current experiments the tip-to-tip separation Δh, was determined to be 600 μm.

Figure 2: Close-up details of dual fiber tips and measurement under a microscope

3.1 Validation of probe velocity measurements using rising bubble experiments and a high speed camera

3.1.1 Description of high speed camera system

In the current experiments, an 8,000 fps frame rate was used to acquire reasonable velocity vector fields. The depth of focus should be minimized because the lens receives the volume-averaged diffraction images. The 60 mm lens with F = 8 was chosen so the estimated depth of focus was shorter than 5 mm.

The focal plane was placed at an offset distance one-quarter the nozzle diameter behind the central plane, to enable sharper bubble images to be obtained. A 12W LED lamp was used as a continuous volume illuminator. Figure 3 is a picture and schematic diagram of the experimental apparatus for making measurements of the size and velocity of passing bubbles showing the camera setup. A circular transparent acrylic cylindrical tank with a diameter of 0.3m was used. In order to prevent the distortion of the image, it was placed in an acrylic rectangular tank filled to an appropriate level with water. Air injection nozzle was placed in the center of the tank bottom with a diameter of 5 mm. Compressed air is supplied to the nozzle via a control valve and the flow rate of the air is precisely controlled by a flow meter. Flow rates of compressed air used were 1, 3, and 5 liter/min.

Figure 3: Experimental setup for probe validation and synchronization timing chart

3.1.2 Analysis of probe signals for bubble velocity and size measurements

Figure 4 shows the time-varying output signal of the fiber optic probe and the corresponding synchronized image from the high-speed camera. Signals obtained first had to undergo filtering to get rid of noise. This was done by setting a cut-off level assuming a 95% confidence level, such that signals outside this threshold are filtered out, and smoother, sharper output signals result.

As shown in Figure 5 (b) it can be seen that the moment the first probe hits the upper boundary of the bubble is 0.1104 s. This indicates a sudden jump in the signal from 0.1 to 1.4 V at the same time stamp. For the second probe this occurs at exactly in the 0.1146 s as recorded by both graph and high speed image. An error of 0.0002 s exists due to the reflected light in accordance with the three-dimensional shape of the bubble as the signal steps-up at 0.1248 before the bubble hits the probe and reaching full steady signal at 0.125 s. At the exit of the probe from within the bubble to the water, the same lag is seen between the signal and the image signal at 0.13 s and 0.1288 s respectively. At 0.135 s there is no reflected light from both probes indicating full exit from within the bubble.

Figure 4: Signals from two optical fiber probes and images taken by synchronized high speed camera.

The time delay Δt between the signals is determined by a cross-correlation algorithm and all computations were done in LabVIEW. Thus, based on the measurement signals from the two probes, the rise velocity of the bubble V_b can be precisely calculated since the probes' separation Δh has been previously determined to be approximately 600 μm as earlier described:

$$V_b = \frac{\Delta h}{\Delta t} \tag{2}$$

In addition, by multiplying the rising speed and the transit time within the gas phase for a

single probe, we can measure the chordal length of the air bubbles. Here, an assumption is that the bubble motion between the probes is uniform; hence, the bubble size can be expressed as:

$$D_b = V_b \times t_r \tag{3}$$

where, t_r is the residence time of the bubble as it traverses a single probe. Bubble size is estimated to within a mean value of 2% error between the two probes. As an example, the size of the bubbles was measured by 3.43 mm from the first probe, was measured to be 3.47 mm in the second probe. A change in length of 0.04 mm while the air bubbles pass through the probes, which is a 1.2% error compared to the average size of the bubble. Three repeated tests of each condition reveal that the maximum of such errors are around 5% with a mean of around 2%. It should be noted that this error estimate was obtained for ideal cases where the bubbles where approximately spherical, and probes penetrate the bubbles at the near the midpoint.

Since length per pixel calibration was done, the bubble speed and size were able to be validated using the images from the high speed camera as given in Figure 4 (b). Results of measuring bubble chordal length at the nozzle exit, and beneath the free surface, as well as mean rise velocities are given in Table 1 for three different inlet air volumetric flow rates.

Table 1: Bubble diameters and rising velocity at different air flow rates

Q_{air} (liter/min)	u_{air} (m/s)	D_b (mm) at the nozzle exit	D_b (mm) below the free surface	V_b (m/s)
1	3.3	12.2	18.1	0.46
3	9.8	16.7	24.2	0.60
5	16.4	21.0	29.6	0.75

As can be seen, the bubble sizes increase with inlet airflow rate, and these consistently grow to 1.5 times their original sizes upon rising to the water surface. This is consistent with their expansion during rise to the lower hydrostatic pressures of the lesser water depths. For the bubble rise velocities, an increase occurs with increase in inlet air flow rates. It can be seen that the air velocity is highly reduced when bubbles are formed on impact with the water due to opposing drag forces within the liquid. However, rise velocity does not increase as fast as inlet velocity. A 5-fold rise in inlet velocity only results in less than 2-fold increase in rise velocity; indicating more dominance by the liquid on bubble properties than those of the gas. Further reading can be done on probe calibration, verification, and general feasibility for use in bubbly flows have been published by the authors in previous papers [21], [22]. Beneath.

4 Ejector experiments and void fraction measurements

Figure 5 (a) shows a schematic diagram of the ejector experimental setup. Metered flow rates of water used as the primary fluid were used to suck (or pump) atmospheric air, the secondary fluid.

The flow rate of air pumped is measured by an air flowmeter (KOBOLD model DOG1102) which was installed at the entrance of the air inlet pipe and has measurement range of 0–0.0083 m^3/s with an uncertainty margin of ±1.5% of measured value. A centrifugal pump circulates tap water stored in a water tank and the inverter is used to control the water flow rate. The water volumetric flow rates used were in the range of 0.0077–0.0092 m^3/s. The water flow rate was measured using an electromagnetic flow meter (KOBOLD model UMF2) which has an uncertainty margin of ±0.3% of full scale measurement. The measured fluid flow rates can be used to determine the gas void fraction (ε_G) in the two-phase mixture as follows:

$$\varepsilon_G = \frac{Q_g}{Q_g + Q_l} \tag{4}$$

where Q_g and Q_l are the gas and liquid volumetric flow rates (in m^3/s) measured by the respective flowmeters. Water enters the gas/liquid ejector, through a strainer and then mixes with air. Downstream of the ejector, bubbly flow results.

Figure 5: Setup for ejector experiments (a) schematic showing ejector loop and measuring devices (b) detailed specification of the annular drive gas/liquid ejector

Pressure measurements were carried out using six 2-wire 4–20 mA output transducers (SUCO model DR-10) with measuring uncertainty of ±0.25% full scale. The notation, location and measurement range of each transducer is as follows: Pi (upstream of ejector) 0–500 kPa; P_i (suction chamber) -10–0 kPa; P_m (center of mixing throat) -10–0 kPa; P_d (outlet of diffuser) -5–15 kPa; P_A (inlet of air pipe) -10–5 kPa; and P_{out} (outlet of visualization section) -5–35 kPa.

In Figure 5 (b), the dimensions of annular drive gas/liquid ejector are given. The inlet and outlet inner diameters are 67 and 69 mm, respectively. The diameter of the ejector venturi neck is 32 mm and the inner diameter of the air inlet, 13.5 mm. The lengths of the converging and diverging sections are 42 mm and 91 mm respectively. In contrast to the conventional gas/liquid ejector, the primary fluid flows annularly around the central air nozzle and air is sucked into the ejector unit.

The high-speed camera (Photron, SA1.1) capable of capturing at speeds of up to 10,000 fps was also installed for the flow visualization with a back illuminator. All measuring devices were connected to an 8-channel National Instruments NI9401 DAQ digital acquisition boards and data captured were logged and stored on a PC. Installation of the optical fiber probe system was done on a traversing device as shown in Figure 6 (a). This facilitates measurements along the radial direction of the horizontal tube.

Figure 6 (b) is an example of filtered instantaneous signals obtained from the two probes at Q_l = 0.0077 m^3/s. Due to the high sensitivity of optical fiber probes in sensing changes in refractive index

between different media, passing bubbles produce clear discrete fluctuations in the measured signals, each signifying the passage of a single bubble. Tiny overlaps can be seen between the two signals and the time stamps are accurately recorded at 8,000 Hz by the LabVIEW DAQ and software, which for 10 s recording, results in 24,000 data points. The void fraction is then determined using an algorithm based on Equation (5) coded in the acquisition software.

Figure 6: (a) Two-channel probe, traversing device, and associated equipment (b) example of instantaneous signals from the two probes during ejector experiments showing distinct detection of passing bubbles at Q_L = 0.0077 m^3/s

The measuring spot was located 0.35 m away from the visualization area, as shown in Figure 7 (a). Associated optical fiber equipment manufactured by Thorlabs Inc. were used: an illuminator to provide a continuous light source (1550 nm, S1FC1550), beam coupler (6015-3-FC), and photodiode (1.2 GHz DET01CFC/M) which converts the reflected light to output voltage signals.

Figure 7: (a) Installed location of the fiber optic probe (b) void fraction determination

To determine the void fraction using the optical fiber probes, signals from a single probe can be used. An algorithm determines a step function $f(t)$ which can only take binary values depending on if the probe is in the liquid phase ($f(t) = 0$) or gas phase ($f(t) = 1$). Therefore, the void fraction is determined by the summation of the areas under the graph of such a function divided by the total length of time ΔT which the signals were acquired. Each area is bounded by the transit time Δt_i through a gas bubble as shown in Figure 7 (b). Hence, as defined [20], [23], the void fraction at a certain radial position for a particular flow condition is calculated as follows:

$$\varepsilon_G = \frac{1}{\Delta T}\int_0^{\Delta T} f(t)dt = \frac{\sum_i \Delta t_i}{\Delta T} \quad (5)$$

Figure 8 shows the radial void fraction distribution as the optical fiber probe vertically traverses the pipe along the radial direction. These were obtained at different water volume flow rates as indicated. The gas void fraction (ε_G) was calculated using $Q_G/(Q_L + Q_G)$ as given in Equation (4). Figure 8 (b) shows the effect of water flow rate on gas pressure. It can be seen that as the water flow rate is increased, the gas backpressure increases and as a result, the void fraction. This is in agreement with the fact that as water flow rate increases, larger pressure drop occurs across the contraction thereby creating more suction at the air inlet to balance the pressure deficit. The average of each measured radial void fraction showed good agreement with that estimated using the volumetric flow rates (See Figure 8 (c)). Due to gas expansion under buoyancy as the bubble rises, the void fraction at bottom was found

to be lower than that at the upper side.

Figure 8: Comparison of the vertical profile of the void fraction (a) different water flow rates at 12 kPa pressure, (b) different gas pressures for Q_L = 0.0087 m^3/s (c) comparison between mean measured values and the calculated values at the different flow rates

4.1 Discussion on ejector bubble velocity and size distributions

Probability density functions (PDFs) were obtained from the bubble velocity measurements for each water volumetric flow rate condition. These are plotted as shown in Figure 9 together with the cumulative distribution function which sums up to unity. Measured bubble velocities varied in the range of 2–5 m/s with increasing peak values as liquid volumetric flow rate increases indicating the liquid being the principal driving phase.

Figure 9: Bubble velocity distribution at y/h=0.3 (P = 12 kPa)

A comparison is made between the measured bubble velocity using the optical fiber probes, the mixture velocity (calculated as $[(Q_L/A_L) + (Q_G/A_G)]$) and the superficial liquid velocity at the aforementioned four Q_L values. Where A_L and A_G are the respective pipe areas for the liquid and gas phases respectively. This is given in Figure 10. The error bars show that the measured velocity by the probes are within 5% of the mixture velocity. The water superficial velocity is an artificial velocity provided that the water phase fully fills the entire cross section of the pipe. On the other hand, in reality air also comprises some portion of the pipe cross-section. Hence, the mixture velocity is always higher than the water superficial velocity. The calculated mixture velocity showed good agreement with the velocity from the optical fiber probe.

Figure 10: Comparison of the measured and predicted axial velocities downstream of ejector

Figure 11 shows the bubble size distribution expressed by the probability density function as well as the cumulative density function. The range of bubble sizes was estimated to range from 1.5 to 6 mm. As can be seen, a variety of bubble sizes were produced by the ejector judging by the multimodal nature of distributions. As stated earlier (see section 3.1.2), penetration through bubbles may not be symmetrical and this can affect the normality of the size distributions. As a result, the shapes of the bubble size distributions in figures (a)–(d) were not similar to that of a standard normal distribution. Also contributing to the given shapes is the small number of samples (25) used to construct the graphs. It is expected that the distributions will approach normality with an increase in sampling size, and this will be implemented in future work.

Figure 11: Bubble size distribution at y/h=0.3 (P_b = 12 kPa)

Mean bubble size decreased with increasing water volume flow rate, as shown in Figure 12. This is expected since higher water flow rate tends to promote bubble breakup. As a result, the gas void fraction also decreases. Therefore, for applications where smaller bubbles promotes increased mass transfer and reaction rates, such as micro-bubble flotation for waste water treatment, liquids should be introduced at relatively high flow rates among other measures [24]–[26]. Conversely, liquid pumping costs will be incurred and a trade-off is involved which may also depend on other factors such as a desired product output flow rate.

Figure 12: Variation of the mean bubble size with respect to Q_L at a pressure of 12 kPa

5 CFD simulation of the ejector setup

In the previous section, the measured void fraction was compared with the gas fraction (ε_G) and good agreement was observed between the values. For additional comparative purposes, CFD analysis using commercially available ANSYS/CFX software was used to simulate the ejector system and to obtain graphical information [27]. The CFX 12.1 User Guide recommended either the Eulerian mixture model or Eulerian particle model is available when analyzing bubbly flows where dispersed-phase volume fractions exceed 10%. Here, the latter was used since fairly well mixed homogeneous bubbly flows inside the ejector and the downstream pipe were observed during the experiments. For initialization, bubble mean diameter was given as 3 mm, based on experimental observations.

The geometry was constructed using the exact dimensions of the experimental setup, and the 3D modeling parts for CFD analysis include ejector unit, visualization chamber and connecting circular pipes. We conducted a mesh dependency study and the optimal number of nodes chosen contained approximately 500,000 nodes. Three-dimensional tetrahedral/prismatic hybrid mesh was used as obtained by ICEM CFD 12.1. In flow setup dialogue, the air was assumed to be incompressible so as not to achieve supersonic speeds. Temperature was fixed as 25°C and air density 1.185 kg/m3. Water was taken as the continuous fluid with air being the dispersed fluid. The k-ω based shear stress transport (SST) turbulence model and dispersed zero equation turbulence model were applied both phases [28]. In the SST turbulence model, wall adjacent cells should be located within the viscous sublayer, and generally recommended to be $y^+ < 1$. For this flow problem, the maximum deviations in the air flow rate predictions between a fine grid ($y^+ = 1$) and coarse grid ($y^+ = 100$) were less than 7%. Ultimately, a fine grid ($y^+ < 10$) was chosen in the air pipe region and coarse grid ($y^+ < 100$) in the two-

phase wall region. Velocity inlet and pressure opening condition with 5% turbulent intensity were applied to water and air as inlet boundary conditions. At the outlet, a pressure outlet boundary condition was applied. For outlet to atmospheric, an additional mesh was created for the simulation of the removed effect caused by the flexible hose connected the downstream elbow. Iterations continued until the residuals for each equation were less than 10^{-4}.

Figure 13 illustrates the CFD results obtained showing contours for the water volume fraction. The section given is the cross-sectional axial view of the ejector system at different water volume flow rates. Gas intake was from atmospheric for all the conditions shown and low pressure regions at the ejector diffuser results in the air being sucked into the pipe by jet pump action. As can be seen, several bubbly flow regions occur, and their propagation length along the tube axis increases with increasing water flow rate. As expected, aeration was greatest at the immediate downstream of gas inlet judging by the void fraction contour and is more so at higher liquid flow rates. This may seem counterintuitive at first. However, it is reasonable considering that the increased velocity of the driving liquid phase means more air can be sucked in; and an elongation occurs of this highly aerated initial bubbly flow region.

Figure 13: Void fraction fields under each operating condition

The stratification of the regions is more apparent when radial cross-sectional views of the results are considered as shown in Figure 14. Cross-sections were examined at four streamwise positions located at the injector inlet, halfway the diffuser, at the entire length of the diffuser, and at an advanced straight tube location. These occur at 1.7, 48, 93, and 740 mm axial locations respectively downstream of the gas inlet. Homogeneous bubbly flow occurs at the diffuser outlet, and as observed earlier, this occurs in several regions. Considering the most developed flow cross-section as shown in Figure 15 (i.e. Section 4 at 0.74 m from the gas inlet), these regions are concentric, but with thicker water volume fractions at the bottom due to the effect of gravity. Initially, three bubbly flow regions occur at the lowest liquid flow rate considered (0.0077 m^3/s). At this condition, water volume fractions range between 0.6 and 0.9 corresponding to void fraction (ε_G) values of 0.1–0.4. The central core of highest value corresponding to $\varepsilon_G \approx 0.4$ widens as the liquid flow rate is increased to 0.0082 m^3/s and it splits into two distinct regions of $\varepsilon_G \approx 0.4 - 0.5$ thus increasing the bubbly flow regions from three to four. Further concentric stratification occurs as liquid flow increases to 0.0092 m^3/s with pipe core peaking of the void fraction. This core-peaking behavior is consistent with the experimental measurements of the void fraction using the optical fiber probes as the profiles given in Figure 8 show. Good quantitative agreement exists between the experimental void fraction and the simulated values. The combined experimental–CFD profiles are given in Figure 15, by comparing the local void fractions at 0.35 m from the air inlet. The coincidence between CFD and experimental local void fractions is very good at the

core region but under-estimations occur towards the wall. These may be due to limitations of the SST model at the boundary layer near the wall at the high Reynolds number conditions of the system and necessity of turbulence damping at the free surface towards the gas–liquid interface [29]. Nevertheless, overall deviation of ε_G between the experiment and CFD is satisfactory.

Figure 14: Cross sectional void fraction distribution at different streamwise locations

Figure 15: Void fraction comparison between the experiment and CFD

6 Conclusion

A dual fiber optic probe system was developed for the measurement of bubble parameters: mean velocity, size, and void fraction in gas–liquid bubbly flows in an annular drive ejector. These are important local parameters that not only enable further understanding of the flow behavior, but are used to obtain physical models of the interfacial area concentration for example, which is useful for the numerical simulation of bubbly flows. Optical fiber probes have the advantage of high sensitivity, and minimal intrusiveness due to their micrometer size, and can be used where other instrumentation are either difficult to deploy or do not give the high temporal resolutions obtainable with fiber optic probes. Experiments were carried out using a PIV method with bubbles as tracer particles to validate the readings of the probes and a high-speed camera system with the capability of 8,000 fps was used. Bubble velocities, and sizes measured by the fiber optic probe showed good agreement with those estimated using the high-speed camera system. Bubble size determination, sizes distributed in range 1.5 to 6 mm were obtained and mean bubble sizes decreased with increasing water flow rate due to bubble break-up by rising wall and gas/liquid shear stresses. Also, void fraction values were obtained using the developed optical fiber probes, and these showed good agreement with the sucked air fraction in the two-phase mixture as measured by a flowmeter. Numerical simulations were also performed for the ejector system using commercial CFD software ANSYS/CFX with the Shear Stress Transport model used for turbulence modelling. The trend of radial void fraction profiles obtained from the numerical simulations closely matched the experimental optical probe values.

Acknowledgement

National Research Foundation of Korea (NRF) funded by the Ministry of Science, ICT & Future Planning (No. 2011- 0030663) and through the MSIP grant GCRC-SOP (No. 2011- 00330013) supported this study. Support was also received from the Basic Science Research Program through the NRF-funded Ministry of Education project (2016R1D1A1A02937232). Finally, we acknowledge the support provided by the BK21 Plus Program of the School of Mechanical Engineering, Pusan National

University, Republic of Korea.

References

[1] A. Ben Brahim, M. Prevost, and R. Bugarel, “Momentum transfer in a vertical down flow liquid jet ejector: case of self gas aspiration and emulsion flow,” *Int. J. Multiph. Flow*, vol. 10, no. 1, pp. 79–94, 1983.

[2] K. Terasaka, A. Hirabayashi, T. Nishino, S. Fujioka, and D. Kobayashi, “Development of microbubble aerator for waste water treatment using aerobic activated sludge,” *Chem. Eng. Sci.*, vol. 66, no. 14, pp. 3172–3179, 2011.

[3] K. Nikiforow, P. Koski, H. Karimäki, J. Ihonen, and V. Alopaeus, “Designing a hydrogen gas ejector for 5 kW stationary PEMFC system – CFD-modeling and experimental validation,” *Int. J. Hydrogen Energy*, 2016.

[4] N. Bilir Sag and H. K. Ersoy, “Experimental investigation on motive nozzle throat diameter for an ejector expansion refrigeration system,” *Energy Convers. Manag.*, vol. 124, pp. 1–12, Sep. 2016.

[5] Y. Mizushima, A. Sakamoto, and T. Saito, “Measurement technique of bubble velocity and diameter in a bubble column via single-tip optical-fiber probing with judgment of the pierced position and angle,” *Chem. Eng. Sci.*, vol. 100, pp. 98–104, Aug. 2013.

[6] K. Akita and F. Yoshida, “Gas Holdup and Volumetric Mass Transfer Coefficient in Bubble Columns. Effects of Liquid Properties,” *Ind. Eng. Chem. Process Des. Dev.*, vol. 12, no. 1, pp. 76–80, Jan. 1973.

[7] S. A. Patel, J. G. Daly, and D. B. Bukur, “Bubble-size distribution in Fischer-Tropsch-derived waxes in a bubble column,” *AIChE J.*, vol. 36, no. 1, pp. 93–105, Jan. 1990.

[8] W. Luewisutthichat, A. Tsutsumi, and K. Yoshida, “Chaotic hydrodynamics of continuous single-bubble flow systems,” *Chem. Eng. Sci.*, vol. 52, no. 21–22, pp. 3685–3691, Nov. 1997.

[9] Y. Fu and Y. Liu, “Development of a robust image processing technique for bubbly flow measurement in a narrow rectangular channel,” *Int. J. Multiph. Flow*, vol. 84, pp. 217–228, Sep. 2016.

[10] Q. Wu and M. Ishii, “Sensitivity study on double-sensor conductivity probe for the measurement of interfacial area concentration in bubbly flow,” *Int. J. Multiph. Flow*, vol. 25, no. 1, pp. 155–173, Feb. 1999.

[11] A. A. Kulkarni, J. B. Joshi, V. R. Kumar, and B. D. Kulkarni, “Simultaneous measurement of

hold-up profiles and interfacial area using LDA in bubble columns: predictions by multiresolution analysis and comparison with experiments," *Chem. Eng. Sci.*, vol. 56, no. 21–22, pp. 6437–6445, Nov. 2001.

[12] S. . Kiambi, A. . Duquenne, A. Bascoul, and H. Delmas, "Measurements of local interfacial area: application of bi-optical fibre technique," *Chem. Eng. Sci.*, vol. 56, no. 21–22, pp. 6447–6453, Nov. 2001.

[13] H.-M. Prasser, A. Böttger, and J. Zschau, "A new electrode-mesh tomograph for gas–liquid flows," *Flow Meas. Instrum.*, vol. 9, no. 2, pp. 111–119, 1998.

[14] A. A. Almabrok, A. M. Aliyu, L. Lao, and H. Yeung, "Gas/liquid flow behaviours in a downward section of large diameter vertical serpentine pipes," *Int. J. Multiph. Flow*, vol. 78, pp. 25–43, 2016.

[15] A. M. Aliyu, A. A. Almabrok, Y. D. Baba, L. Lao, H. Yeung, and K. C. Kim, "Upward gas–liquid two-phase flow after a U-bend in a large-diameter serpentine pipe," *Int. J. Heat Mass Transf.*, vol. 108, pp. 784–800, 2017.

[16] N. Miller and R. E. Mitchie, "Measurement of local voidage in liquid/gas two-phase flow systems using a universal probe," Atomic Power Constructions Ltd., Heston, Eng., 1970.

[17] J. Chabot and H. I. de Lasa, "Gas holdups and bubble characteristics in a bubble column operated at high temperature," *Ind. Eng. Chem. Res.*, vol. 32, no. 11, pp. 2595–2601, 1993.

[18] J. Xue, M. Al-Dahhan, M. P. Dudukovic, and R. F. Mudde, "Bubble Dynamics Measurements Using Four-Point Optical Probe," *Can. J. Chem. Eng.*, vol. 81, no. 3–4, pp. 375–381, May 2008.

[19] J. Enrique Juliá, W. K. Harteveld, R. F. Mudde, and H. E. A. Van den Akker, "On the accuracy of the void fraction measurements using optical probes in bubbly flows," *Rev. Sci. Instrum.*, vol. 76, no. 3, p. 35103, 2005.

[20] D. Morris, A. Teyssedou, J. Lapierre, and A. Tapucu, "Optical fiber probe to measure local void fraction profiles," *Appl. Opt.*, vol. 26, no. 21, p. 4660, Nov. 1987.

[21] G. Kim, S. W. Choi, Y. K. Kim, and K. C. Kim, "Measurement of Bubble Diameter and Rising Velocity in a Cylindrical Tank using an Optical Fiber Probe and a High Speed Visualization Technique," *J. Korean Soc. Vis.*, vol. 10, no. 2, pp. 14–19, Sep. 2012.

[22] S. H. Choi, H. S. Ji, and K. C. Kim, "Visualization of Gas/liquid Ejector Flow and Void Fraction Measurement using Fiber Optic Probe," *J. Korean Soc. Vis.*, vol. 11, no. 1, pp. 34–40, Apr. 2013.

[23] M. Ishii, "Thermo-fluid dynamic theory of two-phase flow," *NASA STI/Recon Tech. Rep. A*, vol. 75, pp. 60–67, 1975.

[24] R. Pérez-Garibay, E. Martínez-Ramos, and J. Rubio, “Gas dispersion measurements in microbubble flotation systems,” *Miner. Eng.*, vol. 26, pp. 34–40, 2012.

[25] V. Martínez-Gómez, R. Pérez-Garibay, and J. Rubio, “Factors involving the solids-carrying flotation capacity of microbubbles,” *Miner. Eng.*, vol. 53, pp. 160–166, 2013.

[26] P. E. Poh, W. Y. J. Ong, E. V. Lau, and M. N. Chong, “Investigation on micro-bubble flotation and coagulation for the treatment of anaerobically treated palm oil mill effluent (POME),” *J. Environ. Chem. Eng.*, vol. 2, no. 2, pp. 1174–1181, 2014.

[27] “ANSYS CFX 12.1 User’s Manual.” 2009.

[28] R. L. Yadav and A. W. Patwardhan, “Design aspects of ejectors: Effects of suction chamber geometry,” *Chem. Eng. Sci.*, vol. 63, no. 15, pp. 3886–3897, 2008.

[29] T. Höhne and J.-P. Mehlhoop, “Validation of closure models for interfacial drag and turbulence in numerical simulations of horizontal stratified gas–liquid flows,” *Int. J. Multiph. Flow*, vol. 62, pp. 1–16, 2014.

Figures

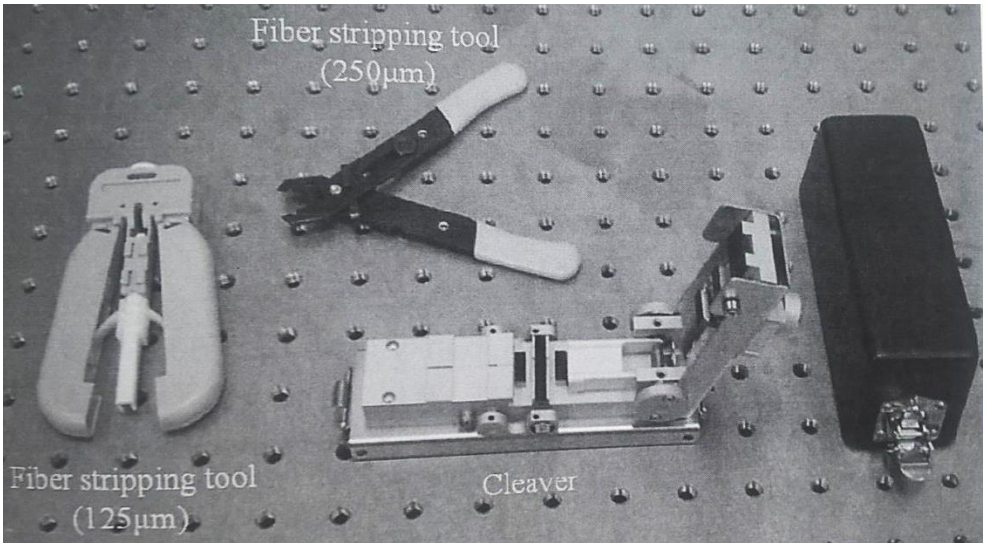

Figure 1: Hand-held precision tools for optical fiber probe fabrication

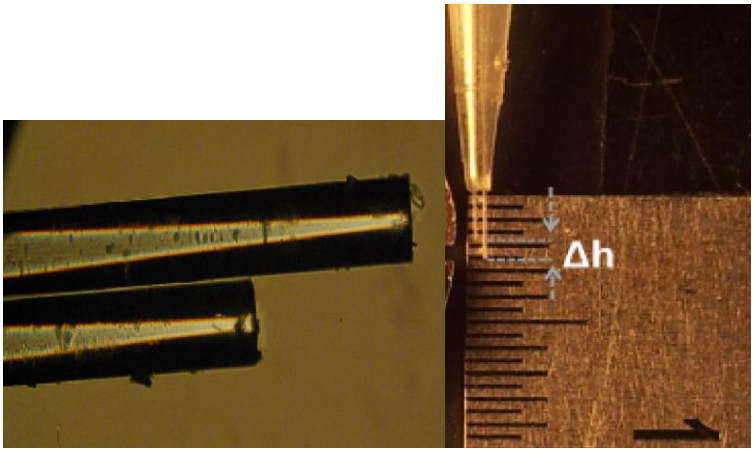

468

469 **Figure 2: Close-up details of dual fiber tips and measurement under a microscope**

470

471

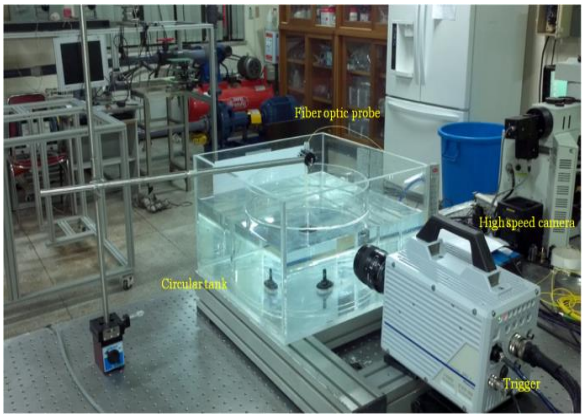

(a) Setup for probe validation

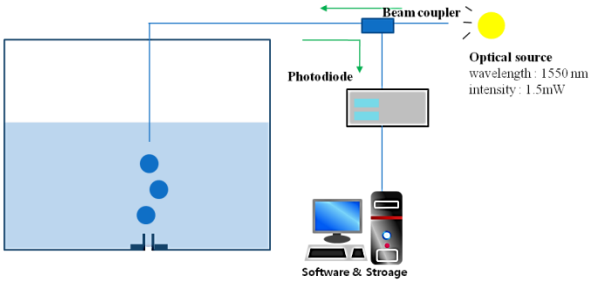

(b) Schematic of setup

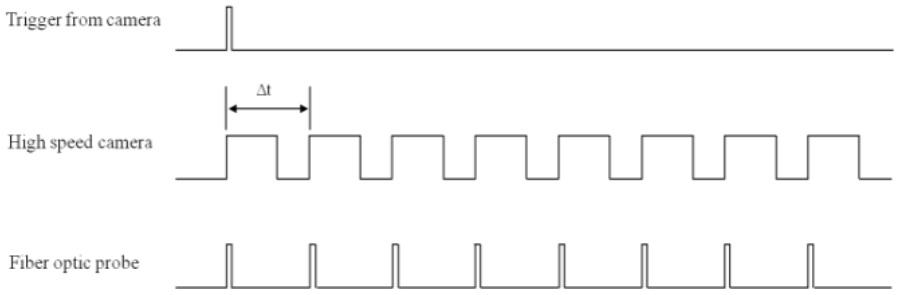

(c) Timing chart for probe and high speed camera synchronization

Figure 3: Experimental setup for probe validation and synchronization timing chart

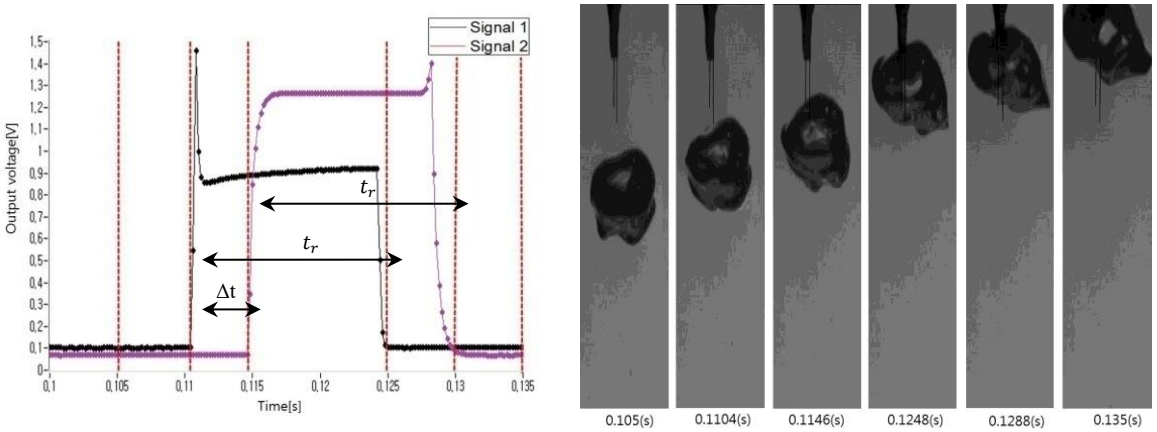

(a) Temporal voltage signal form optical probes

(b) Bubble images taken by the high speed camera

474 **Figure 4: Signals from two optical fiber probes and images taken by synchronized high speed camera.**

475

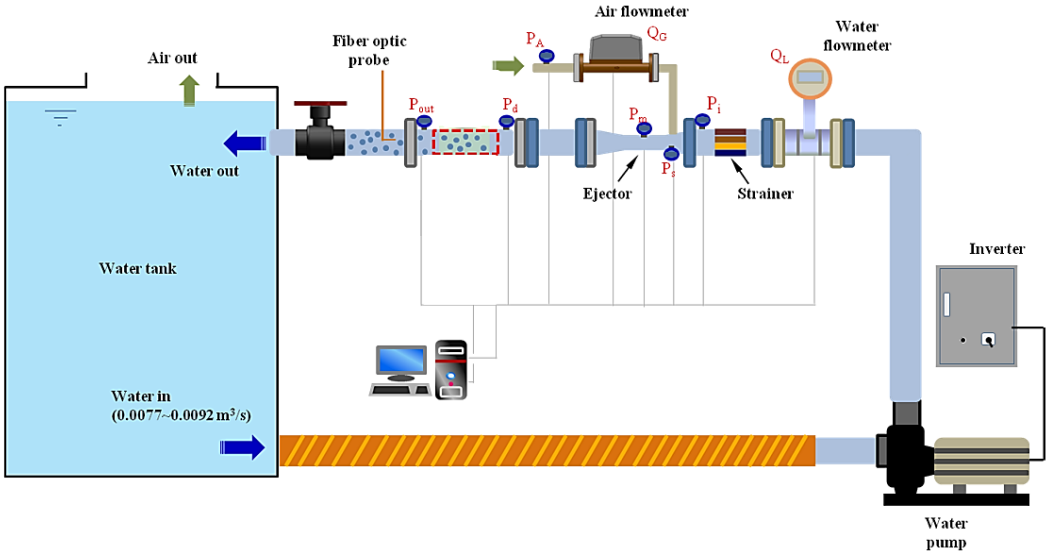

(a)

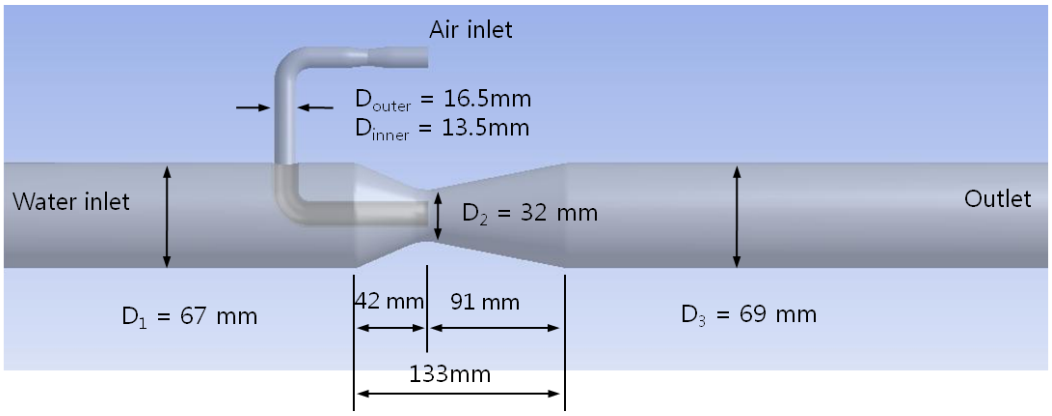

(b)

476 **Figure 5: Setup for ejector experiments (a) schematic showing ejector loop and measuring devices (b)**
477 **detailed specification of the annular drive gas/liquid ejector**

478

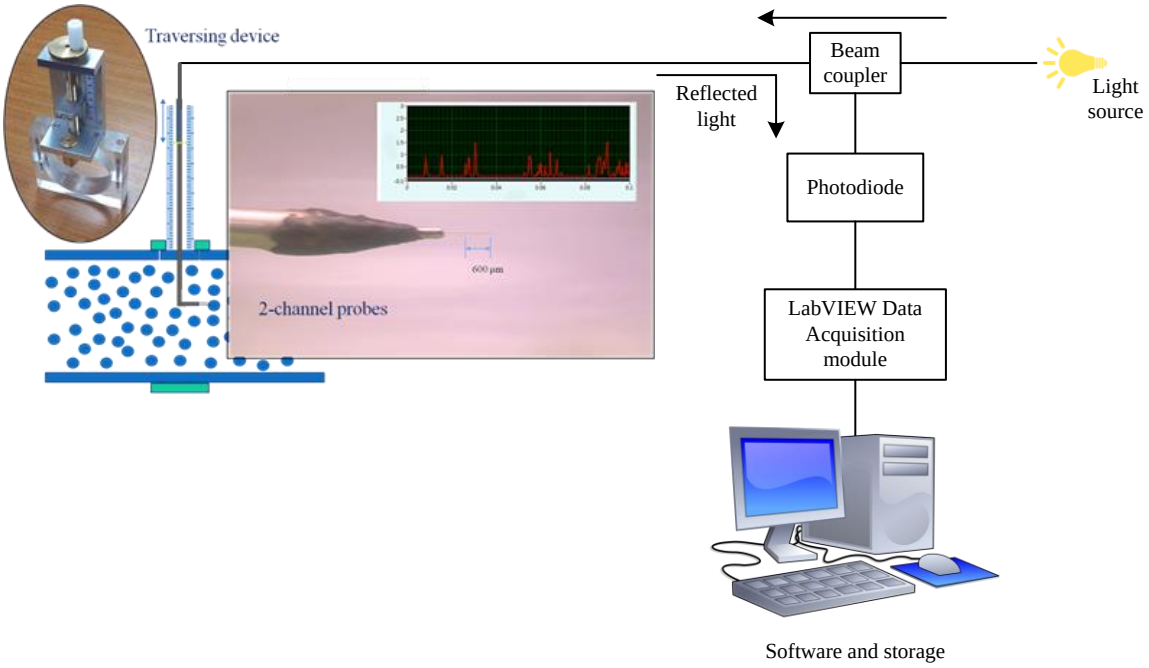

(a)

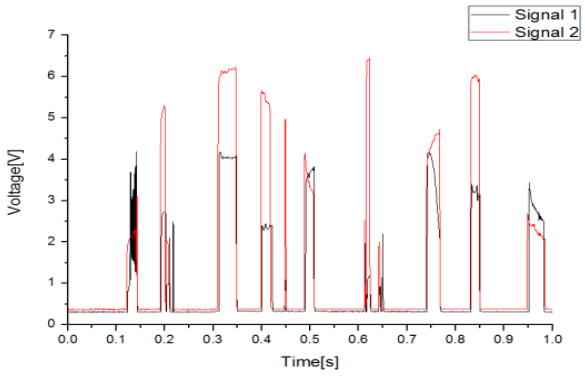

(b)

Figure 6: (a) Two-channel probe, traversing device, and associated equipment (b) example of instantaneous signals from the two probes during ejector experiments showing distinct detection of passing bubbles at Q_L = 0.0077 m^3/s

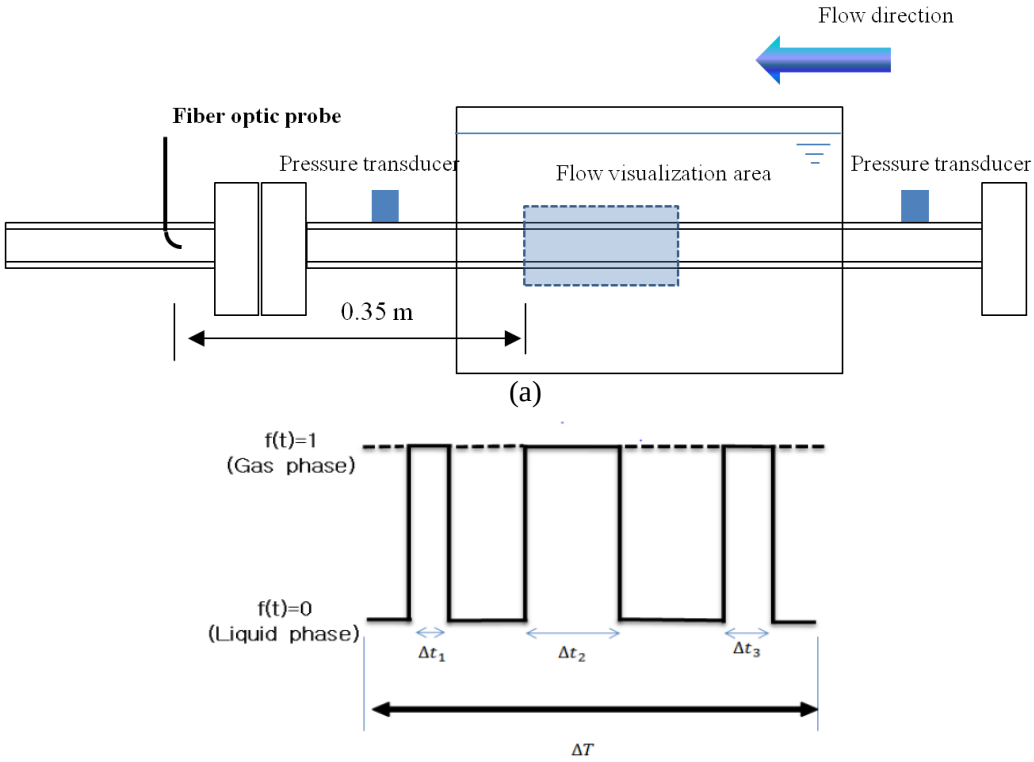

Figure 7: (a) Installed location of the fiber optic probe (b) void fraction determination

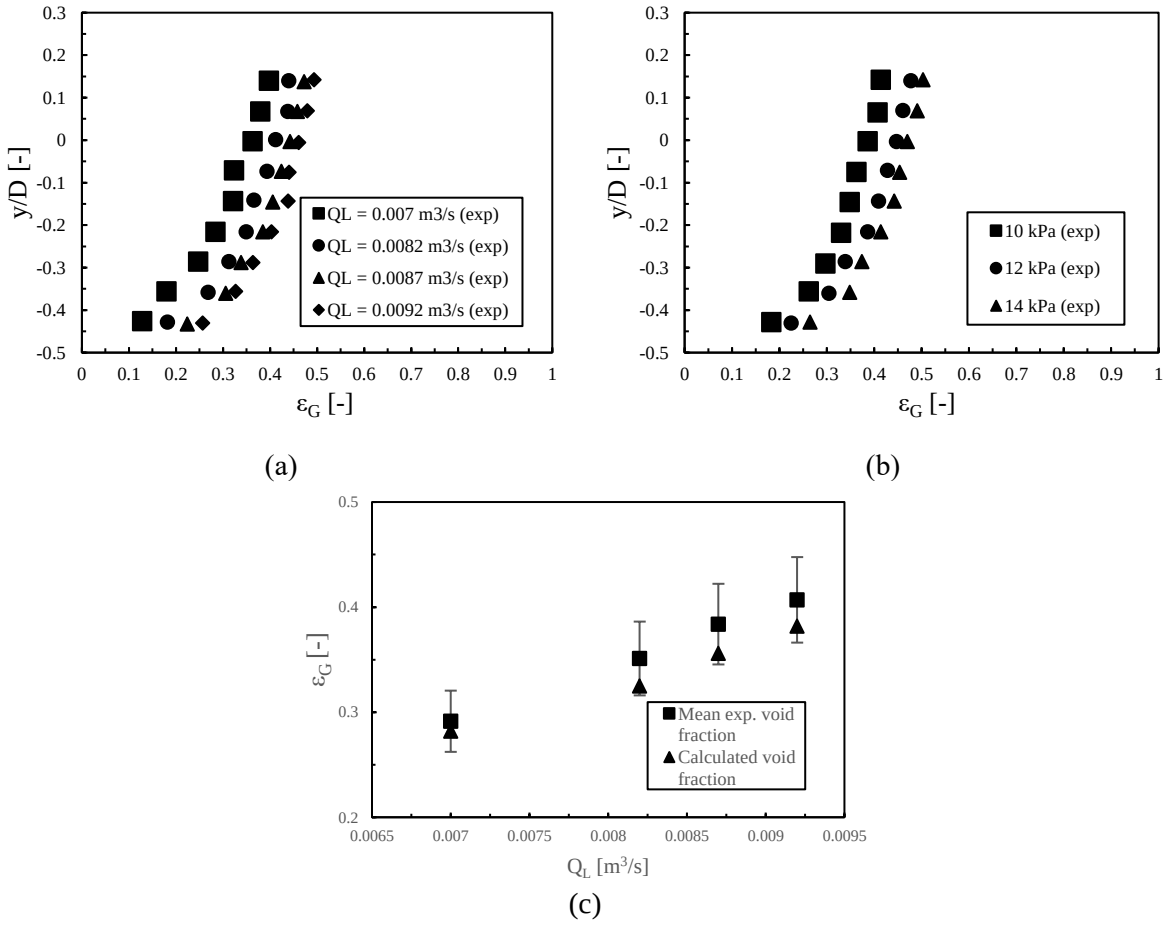

Figure 8: Comparison of the vertical profile of the void fraction (a) different water flow rates at 12 kPa pressure, (b) different gas pressures for Q_L = 0.0087 m^3/s (c) comparison between mean measured values and the calculated values at the different flow rates

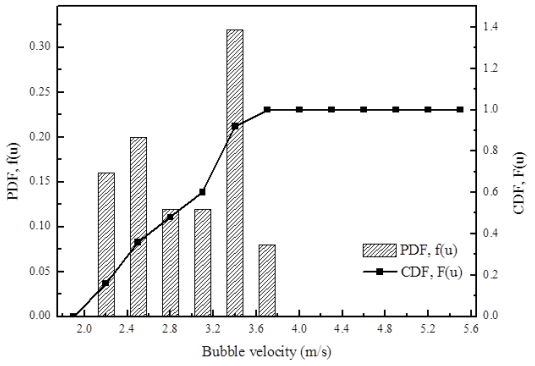

(a) Q_L = 0.0077 m^3/s

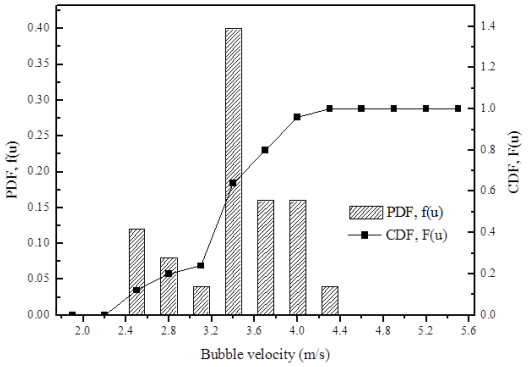

(b) Q_L = 0.0082 m^3/s

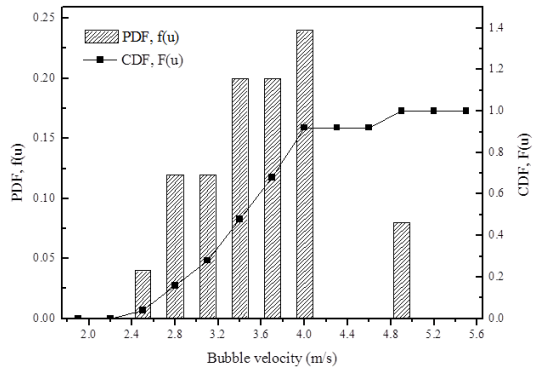

(c) Q_L = 0.0087 m^3/s

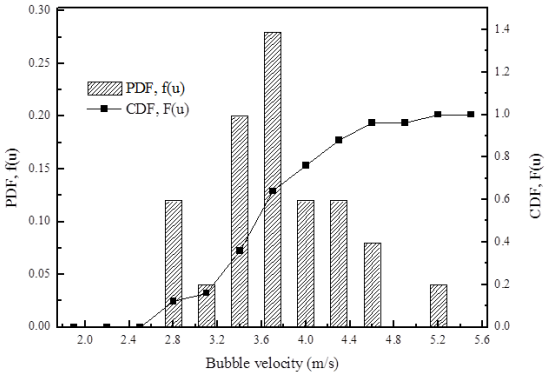

(d) Q_L = 0.0092 m^3/s

492 **Figure 9: Bubble velocity distribution at y/h=0.3 (P = 12 kPa)**

493

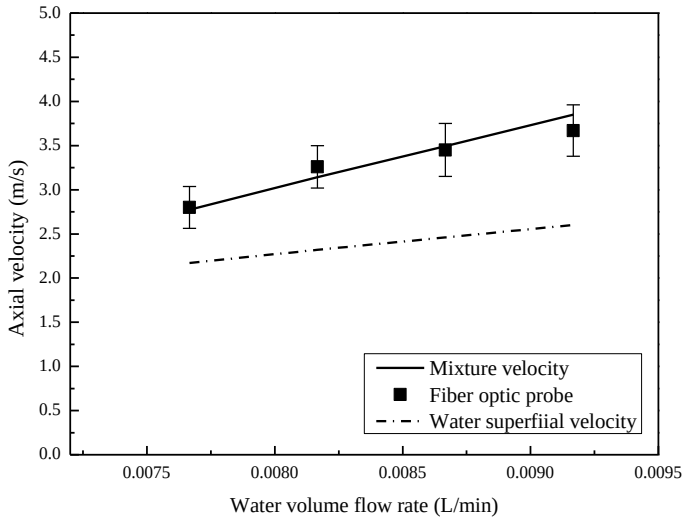

494

495 **Figure 10: Comparison of the measured and predicted axial velocities downstream of ejector**

496

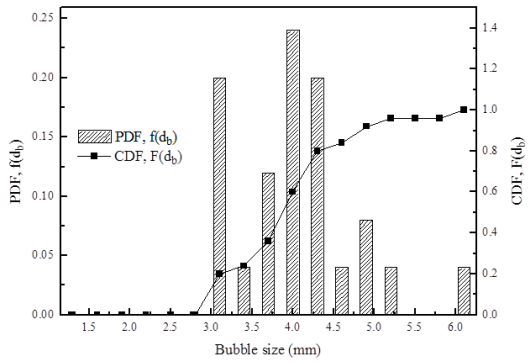

(a) Q_L = 0.0077 m^3/s

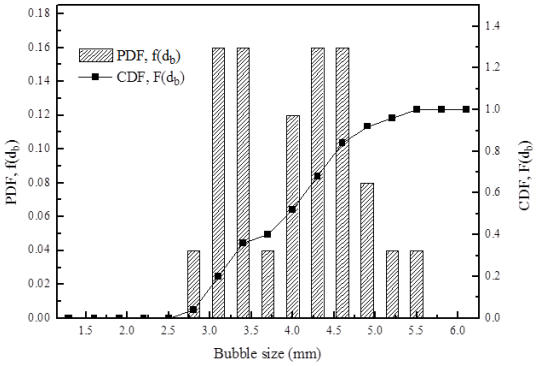

(b) Q_L = 0.0082 m^3/s

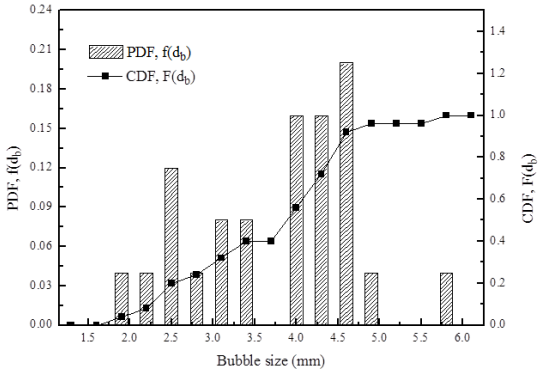

(c) Q_L = 0.0087 m^3/s

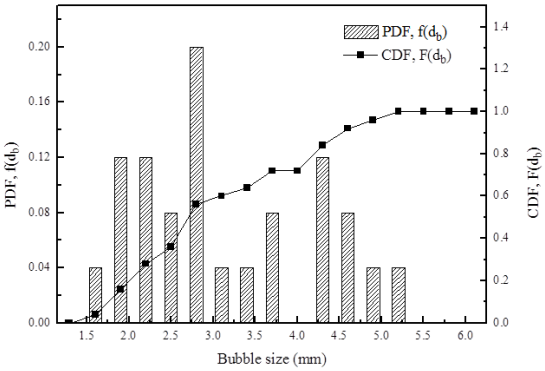

(d) Q_L = 0.0092 m^3/s

497 **Figure 11: Bubble size distribution at y/h=0.3 (P_b = 12 kPa)**

498

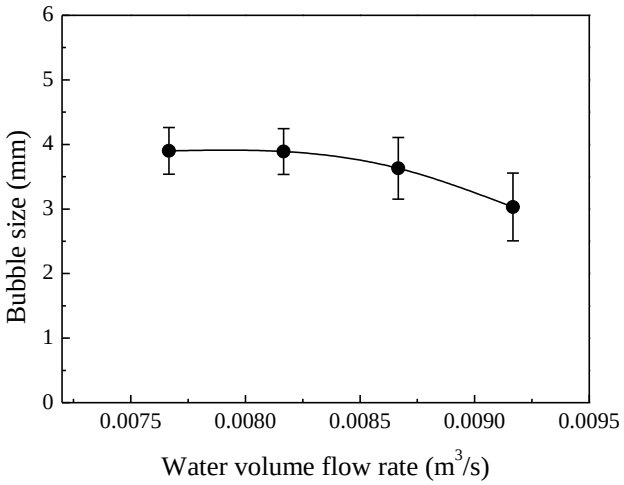

499

500 **Figure 12: Variation of the mean bubble size with respect to Q_L at a pressure of 12 kPa**

501

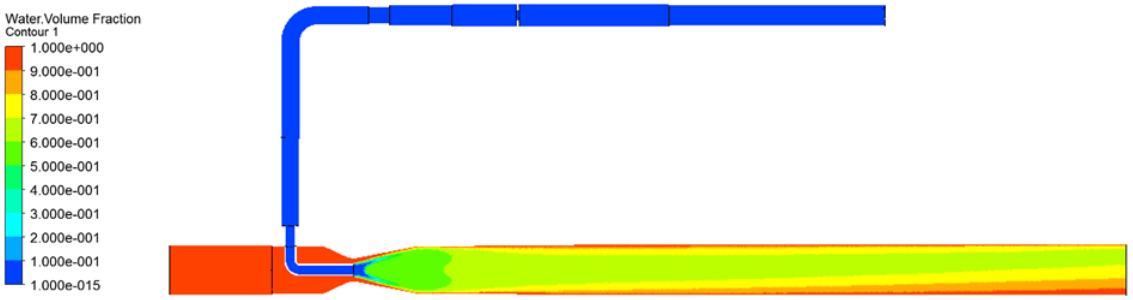

(a) Q_L = 0.0077 m^3/s

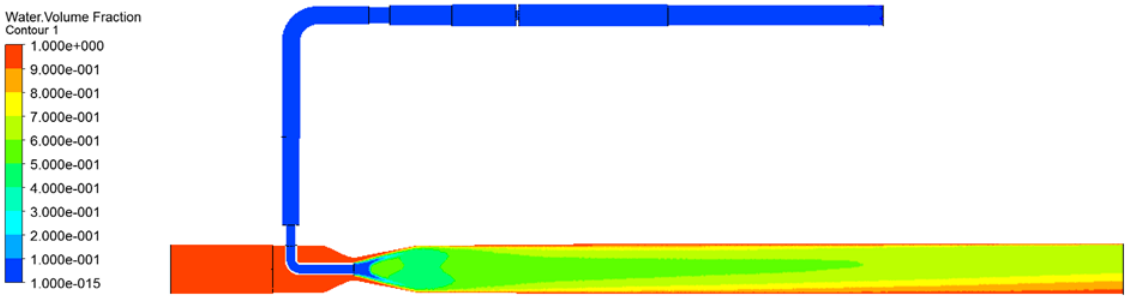

(b) Q_L = 0.0082 m^3/s

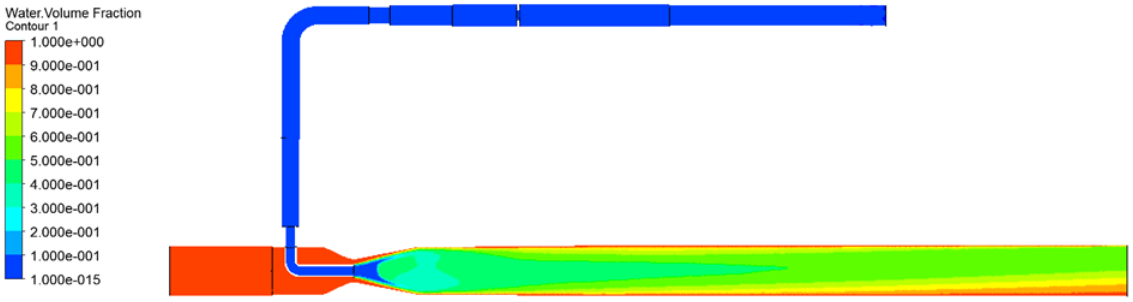

(c) Q_L = 0.0087 m^3/s

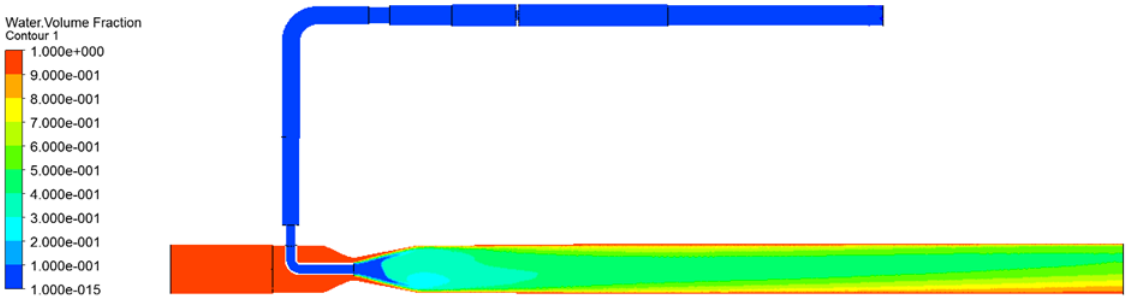

(d) Q_L = 0.0092 m^3/s

Figure 13: Water volume fraction fields under each operating condition

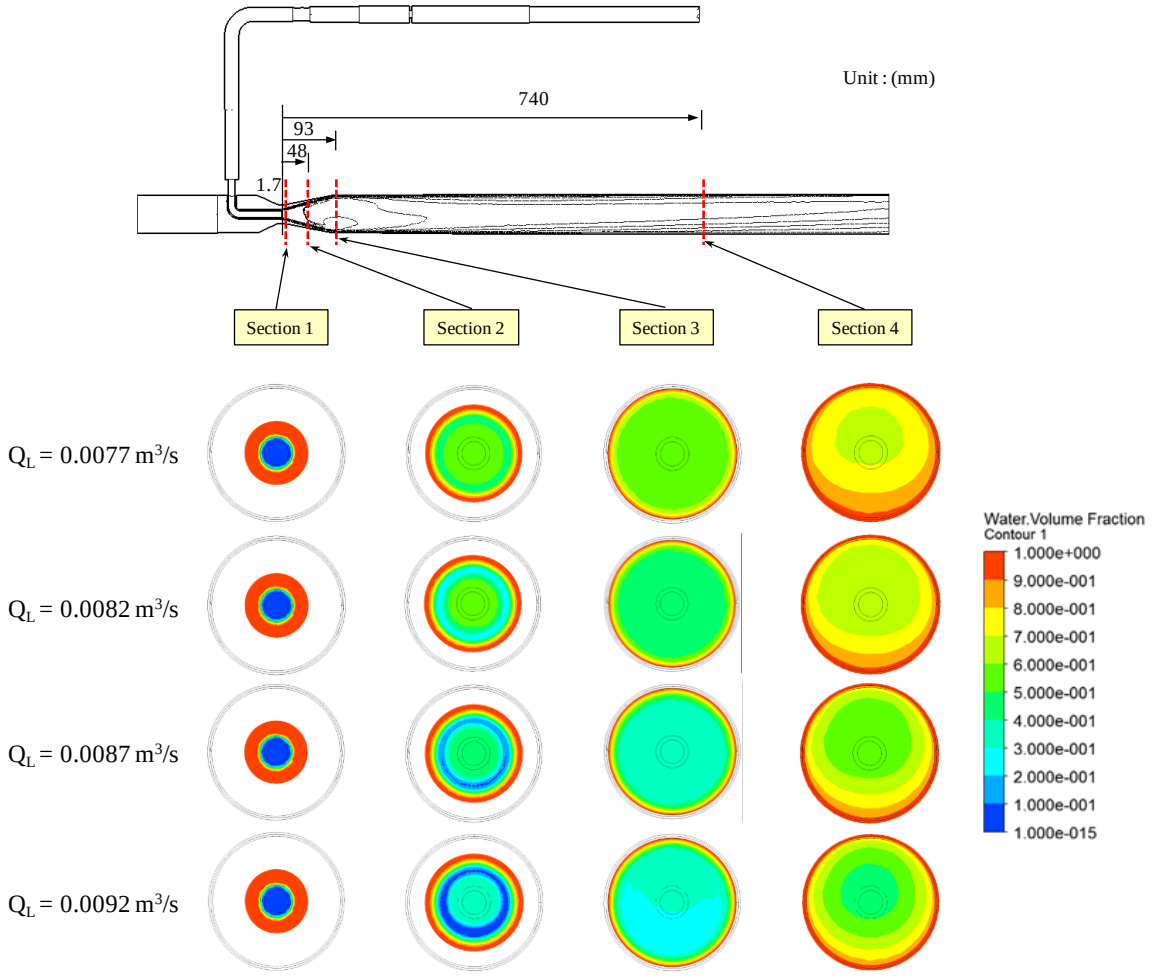

505 **Figure 14: Cross sectional water volume fraction distribution at different streamwise locations**

506

507

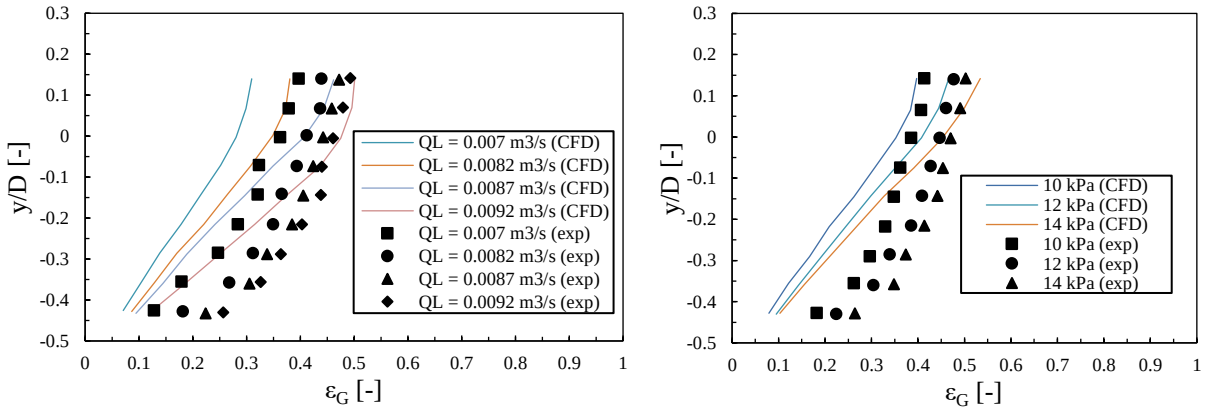

(a) P_b = 12 kPa (b) Q_L = 0.0087 m^3/s

508 **Figure 15: Void fraction comparison between the experiment and CFD**

509

510